



This is a repository copy of *Finite element modelling of surface defect evolution during hot rolling of Silicon steel*.

White Rose Research Online URL for this paper:
<https://eprints.whiterose.ac.uk/id/eprint/141600/>

Version: Accepted Version

Article:

Nioi, M., Pinna, C., Celotto, S. et al. (4 more authors) (2019) Finite element modelling of surface defect evolution during hot rolling of Silicon steel. *Journal of Materials Processing Technology*, 268. pp. 181-191. ISSN 0924-0136

<https://doi.org/10.1016/j.jmatprotec.2019.01.014>

Article available under the terms of the CC-BY-NC-ND licence
(<https://creativecommons.org/licenses/by-nc-nd/4.0/>).

Reuse

This article is distributed under the terms of the Creative Commons Attribution-NonCommercial-NoDerivs (CC BY-NC-ND) licence. This licence only allows you to download this work and share it with others as long as you credit the authors, but you can't change the article in any way or use it commercially. More information and the full terms of the licence here: <https://creativecommons.org/licenses/>

Takedown

If you consider content in White Rose Research Online to be in breach of UK law, please notify us by emailing eprints@whiterose.ac.uk including the URL of the record and the reason for the withdrawal request.



eprints@whiterose.ac.uk
<https://eprints.whiterose.ac.uk/>

Finite element modelling of surface defect evolution during hot rolling of Silicon steel

Nioi¹, M., Pinna¹, C., Celotto², S., Swart², E., Farrugia³, D., Husain, Z.⁴, Ghadbeigi^{1*}, H.

¹ Department of Mechanical Engineering, The University of Sheffield, Sheffield, UK

² Tata Steel Europe R&D, IJmuiden, The Netherlands

³ Swinden Technology Centre Tata Steel R&D, Rotherham, UK

⁴ Warwick Technology Centre Tata Steel R&D, Warwick, UK

*Corresponding author: h.ghadbeigi@sheffield.ac.uk

ABSTRACT

Surface defects on metal strips can be generated during hot rolling from surface cavities and indents. The size and aspect ratio of the initial surface cavities present before rolling are critical parameters that determine the final configuration of the defect. The propagation of these defect through the full rolling process is detrimental to the surface quality of the end product, in particular for electrical steel where these type of defects may directly affect the magnetic properties of the final product. A finite element model was developed in the present research to simulate the evolution of surface defects in a high-silicon electrical steel subjected to a single pass hot-rolling operation. The surface defects were modelled as predefined cavities with various aspect ratios and a multi-scale approach was used to capture the large local deformation gradients at the vicinity of the initial cavities. A user-defined subroutine was developed to describe the material constitutive behaviour at different strain rates and temperatures based on the Sellars-Tegart model in ABAQUS/standard finite element package. The modelling results were validated by laboratory scale hot rolling experiments with respect to the measured rolling forces and the plastic deformation of the initial cavities. This study shows that buckling of the lateral sides and bulging of the floor of the initial cavities are the main mechanisms involved in the formation of sub-surface defects. The developed model can be used to predict the evolution of surface cavities and to optimise the rolling parameters in order to minimise the detrimental effect of these defects in the final stages of the hot rolling process.

Key Words: Hot Rolling, Surface Defect, Modelling, Deformation, Electrical steel.

Nomenclatures

$\dot{\epsilon}^{pl}$	Plastic strain rate vector (s^{-1})	α	Material constant (MPa^{-1})
Θ_{AMB}	Average surface temperature (K)	A	Material constant (s^{-1})
Θ_{AVG}	Ambient temperature (K)	Pfr	Rate of frictional energy dissipation
Θ_a	Temperature point a (K)	Q	Hardening constant (MPa)
Θ_b	Temperature point b (K)	R	Universal gas constant ($\frac{kJ}{mol \cdot K}$)
Θ^z	Absolute zero temperature (K)	T	Temperature (K)
q_s	Heat generated by friction (kJ)	b	Hardening constant
r^{pl}	Heat generated per unit of volume due to plastic deformation	f	Fraction of converted heat distributed in the surface
$\dot{\gamma}$	Slip rate (s^{-1})	p	Surface pressure (MPa)
$\dot{\epsilon}$	Strain rate (s^{-1})	ϵ	Strain
σ_{S-B}	Stefan-Boltzmann constant	ϵi	Emissivity of the surface
σ_s	Ultimate tensile stress (MPa)	η_p	Fraction of plastic work converted to heat
τ_c	Critical shear stress (MPa)	η_f	Fraction of frictional work converted into heat
τ_{lim}	Shear limit (MPa)	μ	Friction coefficient (MPa)
ΔH	Activation energy for plastic deformation ($\frac{kJ}{mol}$)	σ	Stress level (MPa)
k	Gap conductance ($\frac{kW}{m^2 \cdot K}$)	τ	Frictional stress (MPa)
q	Computed heat flux ($\frac{kW}{m^2}$)	σ	Stress vector (MPa)

1. INTRODUCTION

The manufacturing of flat metal products typically involves a hot rolling process stage. Hot-rolling is performed with the work-piece heated to sufficiently high temperatures to reduce its strength. This has the advantage of enabling significant thickness reductions without damaging the workpiece as well as reducing the forces on the rolls. However, high-temperature processing has the disadvantage of increasing the likelihood of surface defects due to the softer work-piece indenting more easily and due to ubiquitous oxide scale formation. In some instances, the scale within indents may become buried during sequential rolling operations and re-emerge at later processing stages. This may adversely affect the functionality, integrity and aesthetic appearance of the final product. In this context, a reliable modelling strategy to accurately predict the deformation of surface indentations during rolling and to understand evolution mechanisms of these features would assist in developing process strategies to prevent such defect forming phenomena.

Some attempts have been made to understand the evolution of surface indentations with different geometrical configurations; Lee and Choi (2008) simulated the evolution of 2D square cavities and concluded that the width to depth ratio of the initial defects on the slab surface determines the pattern of the final surface. Yu and Liu (2016) developed a model to predict the evolution of 3D transversal surface cracks on the surface of slabs subjected to hot rolling operations and reported that the final crack height increases with the initial crack height and with the decreasing opening angle and friction coefficient. Yu *et al.* (2008) carried out a similar analysis on the evolution of inclusions in stainless steel slabs where in both the studies it was found that friction plays a crucial role on the defect deformation during rolling. Nioi *et al.* (2017) in an experimental study on silicon steel found that the geometry of the initial features, the material properties and the rolling parameters, such as the coefficient of friction, play a role on the deformation and evolution mechanisms of defects in silicon steel.

Friction conditions and heat transfer are the boundary conditions affecting the interaction between the roll and the slab during the hot rolling process and both are strictly dependent on the oxide scale present between roll and slab. Several studies carried out to understand the properties and the behaviour of oxide scales formed during rolling including the one reported by Li and Sellars (1998) investigated the influence of oxide scales on the heat transfer behaviour during forging and rolling. It is reported that the oxide cracking greatly influence the overall heat transfer condition at the interface. Chen and Yuen (2001) studied the oxide structures of hot rolled strips wherein the results highlighted the significant increase of oxide thickness with the coiling temperature. Grenier *et al.* (2008) also investigated the fracture phenomenon of oxide scales during hot rolling and reported that cracks form due to the stress concentration. Takeda *et al.* (2009) studied the properties of Si oxide at high temperature and determined the conductivity, the hardness and thermal expansion for different oxide structures. Onishi *et al.* (2010) carried out some research on the physical properties of iron oxide scale on silicon steel, and determined the rate constants of oxidation. Suárez *et al.* (2010) studied the oxidation of low carbon and silicon steel at high temperatures concluding that the presence of fayalite (FeO_2SiO_2) promote the rapid grow of oxide on silicon steel by liquid oxide attack. Song *et al.* (2012) modelled the oxidation of silicon steels and concluded that even for large silicon concentration, the iron oxide represents the dominant scale component.

The influence of oxide scales at high temperatures on friction and heat transfer has also been reported. The oxide scale layers can act as a lubricant or abrasive depending on their thickness, temperature and chemical composition. Munther and Lenard (1999) carried out an investigation of the effects of oxide scales on friction during hot rolling processes and concluded that thicker scale thickness produces lower friction coefficients providing some degree of lubricity. Utsunomiya *et al.* (2009) in their research on the deformation of oxide scale during hot rolling obtained analogous results, finding that the friction decreases with the scale thickness when the scale does not deform uniformly.

Regarding the thermal behaviour of oxide scales, Sun (2005) in a study on silicon steels, demonstrated that a thick oxide layer can form a thermal barrier due to its lower thermal conductivity compared with the steel, reducing the heat transfer coefficient between the roll and the slab.

Silicon steels are widely used in electrical applications in the form of very thin gauge laminations (in the order of few hundreds of microns) due to their enhanced magnetic properties compared to other steel grades. The high Si content results in predominantly ferritic microstructure during hot-rolling that is relatively soft. This can be easily verified by comparing the stress saturation levels of silicon steel grades (Rodriguez, 2014) with general low carbon steels (Baragar, 1987). To the best knowledge of authors, only a few studies conducted to predict mechanical properties of silicon steel, with up to 2 wt% silicon, at both high temperatures and strain rates for different manufacturing operations. Brown *et al.* (1989) proposed a model with an extra state variable to represent constitutive behaviour for hot working of metals, a good match was found between simulation and experiments. Rodriguez *et al.* (2014) introduced a modified hyperbolic function to derive stresses at different strain rates and temperatures for silicon steels of different grades.

The studies found in the literature related to modelling of indentation evolution during hot rolling of metallic materials are limited to 2D features representing rectangular shapes with two principal dimensions as the study carried out by Lee and Choi (2008). However, this simplification may not represent the true three-dimensional geometry of real surface defects and its evolution during hot rolling. For this reason, a more rigorous description of the geometric evolution of the defects during the process is needed.

Moreover, the evolution of defects during rolling in electrical steel has never been studied. Considering the reduced mechanical resistance of the material at high temperatures with respect to other steels and the high surface quality standard required for its application, a detailed study of defect evolution of this material is required.

In the present research, a material model is calibrated and implemented into a commercial finite element package to predict the three-dimensional evolution of surface cavities in a hot rolling process of a 3 wt%Si electrical steel, using a multi-scale three-dimensional modelling strategy.

The simulations are conducted for a series of controlled rolling experiments where slabs containing indentations of different geometries with various aspect ratios are used to analyse the cavity deformation. The modelling results are validated based on the measured roll forces, plastic deformation of the rolled material and the measured length, width and depth of the deformed cavities.

2. MODELLING STRATEGY

A laboratory rolling experiment, described in (Nioi *et al.*, 2017), was modelled. Slabs 115mm x 85mm x 25mm in size, containing artificial surface cavities, were rolled using a lab-scale mill with 223mm-diameter rolls. The initial thickness to width ratio was such that a three dimensional deformation state was imposed during rolling. The rolling operation was modelled as a fully-coupled thermo-mechanical process, with the rolls considered as rigid bodies and the temperature as the only degree of freedom. The slab was assumed to be deformable with temperature and strain rate dependent material properties implemented through a user-defined subroutine (UMAT) using Abaqus/Standard 6.13-1 solver (2013). A multi-scale modelling strategy using the sub-modelling option available in ABAQUS and including both a macro and meso-scale model, was adopted to account for the large difference between the size of the rolled slab and the defect cavities (in the order of several millimetres). Using this strategy, an optimal computationally-effective mesh morphology in the defect zone was achieved helping to reduce the computational time. The macro-scale model was used to simulate a single rolling pass without any surface defect. The local boundary conditions of a selected volume of the material were transferred to the meso-scale model containing the initial cavities prior to the rolling operation. This methodology helped analyse the deformation of cavities of different geometries without the need of running a full model of the process containing the defect. The term “cavity” will be used to refer to the artificially designed holes present in the slab before rolling and “defect” to refer to the deformed features during or after rolling. In the current research, the effect of oxide scale was incorporated into the friction coefficient value, which is explained in the following sections. It was assumed that the thin oxide layer that forms immediately after descaling, does not affect the thermal conductivity of the material.

2.1. Material model for 3wt% Si-electrical steel

Eq.(1) is used to describe the flow stress of the material, as a function of temperature and strain rate, for a given ultimate compressive stress ($\sigma_s(T, \dot{\epsilon})$) and plastic strain level.

$$\sigma = (\sigma_s(T, \dot{\epsilon}) - Q) + Q \cdot \sqrt{1 - e^{-b \cdot \epsilon}} \quad (1)$$

where Q and b are material constants related to the strain hardening of the material and ϵ is the equivalent plastic strain. It was assumed that Q and b are not dependent on the temperature and strain rate.

The Sellars and Tegart (1972) temperature-displacement coupled material model Eq.(2) is widely used for formulating experimentally measured constitutive behaviour of materials (Tello *et al.*, 2013) based on the prediction of the ultimate compressive stress of the material (σ_s) at specific temperature and strain rate conditions.

$$\sigma_s = \sin^{-1} \sqrt{\frac{\dot{\epsilon} \cdot e^{\frac{\Delta H}{RT}}}{A}} \cdot \frac{1}{\alpha} \quad (2)$$

In Eq.(2), A (s^{-1}), α (MPa^{-1}) and n are material constants. The other parameters are further explained in the nomenclature section. The four parameters A , α , n and ΔH were determined using a numerical technique proposed by Uvira and Jones (1968). The material constants Q and b were determined by fitting the experimental data of the flow curves using a least square method. The elastic modulus was defined as a function of temperature according to the values provided by Brown *et al.* (1989) for a similar silicon steel. The thermal conductivity was fixed to $60 \frac{W}{^{\circ}K \cdot m}$.

2.2. Thermal conduction and heat generated due to plastic deformation

The thermo-mechanical contact condition with thermal conduction between the roll and the slab was implemented in the model. Conductance is introduced as a contact property and it was described by Eq.(3):

$$q = k \cdot (\theta_a - \theta_b) \quad (3)$$

where q is the heat flux per unit area that crosses the surface from point a , with a temperature of θ_a , to point b having a temperature of θ_b . The contact conductance (k) was fixed to $20 \frac{kW}{m^2 \cdot K}$ according to the formulas provided in the extensive research on oxide scale behaviour during rolling carried out by (Krzyzanowski *et al.*, 2010).

It was also assumed that 95 % of the mechanical work is converted to thermal energy according to (Shangwu *et al.*, 2001), resulting in added heat flux to the rolled slab. This additional heat flux was implemented according to Eq.(4) where the heat flux per unit of volume is calculated as:

$$-r^{pl} = \eta_p \cdot \sigma : \dot{\epsilon}^{pl} \quad (4)$$

where $-r^{pl}$ is the computed heat flux generated per unit of volume due to plastic deformation and η_p represents the fraction of plastic work converted to heat ($\eta_p = 0.95$). The stress and strain rate vectors are denoted by σ and $\dot{\epsilon}^{pl}$ respectively.

2.3. Friction

The interaction between the roll and strip surfaces was simulated using the classical isotropic Coulomb and stick-slip friction model (Lenard, 1990) Eq.(5). It was assumed that sliding at the contacting surfaces occurs when the equivalent shear stress at a contact point exceeds the critical shear stress value (τ_c) defined by the coefficient of friction (μ) and the contact pressure (p). The shear strength of the material at the vicinity of the contact surfaces (τ_{limit}) was used as the upper-bound limit for the tangential stress along the contacting surfaces.

$$\tau_c = \mu \cdot p$$

(5)

According to studies carried out on similar electrical steel grades (Brown *et al.*, 1989), it was also assumed that 90 % of the frictional work is converted to heat that is equally transferred to the slab and the roll at the contact point.

3. GEOMETRIES, MESH MORPHOLOGY AND BOUNDARY CONDITIONS

3.1. Macro-scale model

The rolls were modelled as rigid half-rings, with a radial thickness and width of 15 mm and 120mm respectively, that are constrained to rotate around their axes. The radial thickness was defined to guarantee a thermal gradient in the roll. The rolls were intentionally designed to be wider than the slab (with an initial width of 87.5mm) in order to replicate the boundary conditions of the selected hot rolling process and to ensure that the frictional contact assumptions are valid for the laterally expanded material due to the compressive deformation. Contact was defined between the roll surfaces and the top and bottom surfaces of the slab using a surface-to-surface discretization method. An initial translational velocity of 0.035 m/s and a rotational velocity of 19 rpm were applied to the slab and the roll respectively, to replicate the test conditions that will be presented later in the text.

The rolling gap was adjusted to obtain a 40% reduction. Reduced integration hexahedral coupled thermal-stress elements (C3D8RT) were used to mesh the rings, Figure 1. The selected elements are 10mm, 6.5mm and 5.7 mm in the transversal, tangential and radial directions respectively. Reduced integration thermal-stress coupled hexahedral elements (C3D8RT) with hourglass control were used to mesh the slab. In order to address the shear locking phenomenon due to excessive plastic deformation and improve the computational efficiency, the artificial hourglass stiffness was estimated as a function of the shear modulus as recommended in the Abaqus documentation for solid elements (Abaqus 6.13-1, 2013). A vertical symmetry plane was considered to model the half-width of the slab (Figure 1a) in order to reduce the computational time. The hourglass control helps to avoid the shear locking effect due to an excessive deformation in the elements. Finer elements were used at the top and bottom contacting surfaces of the slab to address the expected large deformation gradient in the contact zones (Figure 1b). A mesh convergence study was carried out to ensure the results are not dependent on the elements dimension.

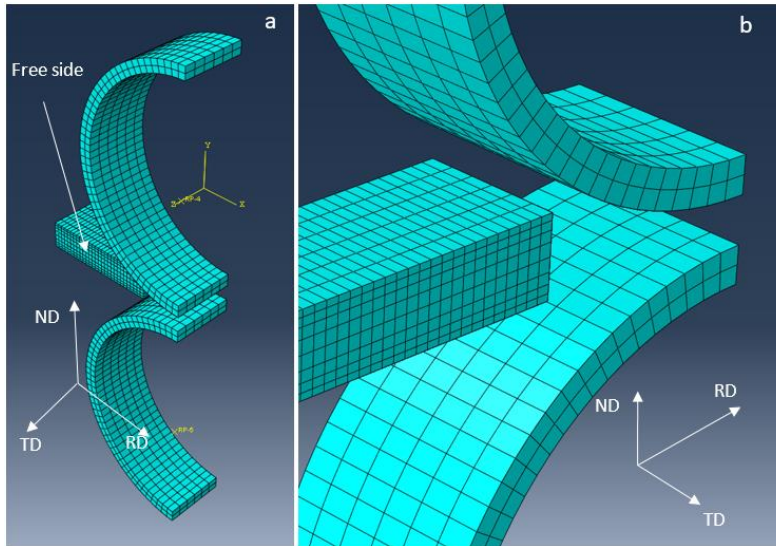


Figure 1: (a) Macro-scale model mesh, and (b) enlarged view of the element dimension in the contact zone.

3.2. Mesoscale model

The meso-model is a sub-volume of the macro-scale model that includes a selected portion of the slab containing a cavity located on its top surface. Figure 2 shows an example of a meso-scale model (Figure 2a) with the enlarged part of the slab containing a cavity (Figure 2b). The cavity should have a negligible effect on the stress and temperature fields at the boundary of the meso-scale model in order to correctly transfer the results of the macro model to the meso-scale model. Consequently, a parametric study was performed to determine the length of the meso-scale model. This was done to achieve dimensionally independent stress and temperature fields at the boundaries of the selected sub-volume in the meso-model. The calculated fields should be identical to those obtained from the macro model at the boundaries of a sub-volume with similar dimensions. The meso-scale model and a sub-volume of macro-scale model with a length of 50 mm, longer than the projected length of arc of contact, was selected for the multi-scale analysis of all the selected cavities. The obtained nodal thermal and displacement fields of the macro-scale model at the boundary of the selected sub-volume (shown by red arrows in Figure 2a) were then applied to the meso-scale model as the initial boundary conditions, forcing the selected section to follow the deformation field around the cavity and those imposed by the contact with the rigid roll.

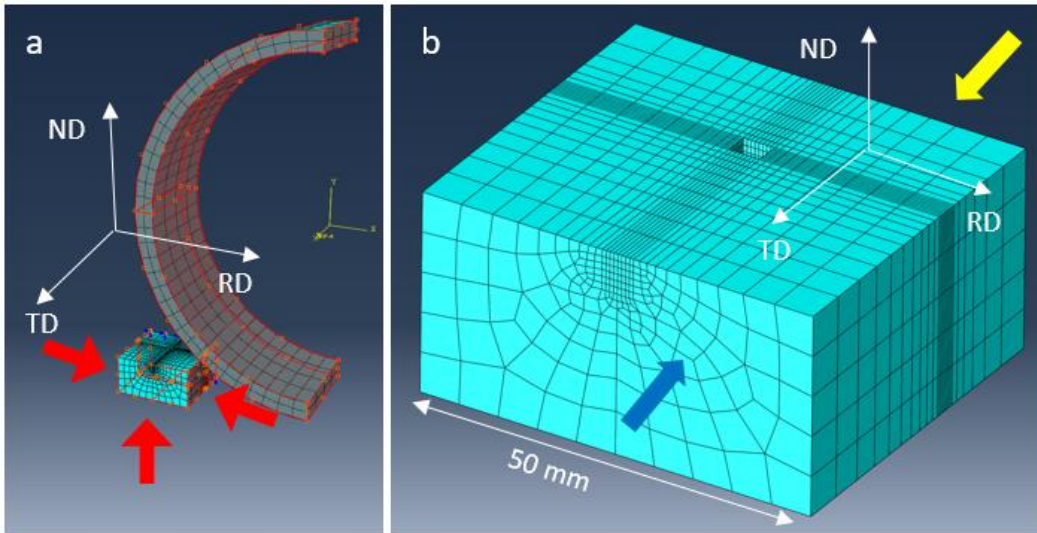


Figure 2: Meso-scale model and boundary conditions applied, a) boundary conditions applied highlighted in red, b) sub-volume detail mesh scheme of the slab containing a generic surface cavity.

The yellow arrow in Figure 2b indicates the plane of symmetry and the free lateral side of the meso-scale model is shown by the blue arrow. The cavities were located at identical positions to those designed in the rolling experiment that was carried out to validate the model (Nioi *et al.*, 2017). Progressive mesh refinement was used to improve meshing quality using structural elements with an aspect ratio of 1:1:1 at the vicinity of the cavities as shown in Figure 2b. A mesh convergence study indicated that a minimum number of six elements in the normal direction of the cavities (ND in Figure 2b) was sufficient to avoid mesh dependency of the deformation for all the cavities considered. Contact was defined between the internal sides of the cavities and between slabs and roll surfaces to simulate their interaction during deformation using a surface-to-surface discretization method.

Five cavities with different aspect ratios (Table 1) were selected from a list of those tested in the hot rolling experiments. Those selected geometries represented average values of length (10mm) and width (7mm) for different depths (1mm, 3mm, 5mm) and the extreme combination of length/width ratios for the average value of depth (3mm) of the cavities used in the experiments.

Table 1: Cavity dimensions for the defect analysis and validation. D , L , and W represent the depth, length and width of the cavities respectively.

Cavity N°	L_i (mm)	W_i (mm)	D_i (mm)
1 (H1)	10	7	1
2 (H2)	10	7	3
3 (H3)	10	7	5
4 (D2)	4	11	3
5 (C2)	17	3	3

The model and sub-model run using Abaqus/Standard 6.13-1 on a Windows 64 workstation with the CPU times of 24 hours for the macro-scale model (1928 nodes) and about 8 hours for the meso-scale

model (4656 nodes) depending on the defect dimensions using an Intel® Xeon® Processor E5-2650 v2 (eight core HT, 2.6 GHz Turbo, 20 Mb).

4. EXPERIMENTAL VALIDATION

The hot rolling experiments results reported in (Nioi *et al.*, 2017) were used to validate the model where slabs of 25 mm in thickness were rolled with a rolling radial velocity of 19 RPM (corresponding to a tangential velocity of 0.035 m/sec). A reduction of 40% was achieved in a single rolling pass and roll forces were recorded. Cavities with different dimensions were machined on the surface of the six slabs. In addition, stainless steel pins were inserted through the slabs perpendicular to the rolling plane. These enabled the deformation through the thickness to be quantified. Figure 3 shows an example of a slab containing cavities used in the experiment, where three pins inserted in the slab are highlighted in red and the plane of symmetry is highlighted with a white dashed line. The pins inserted in the slab were cut in the longitudinal direction in order to assess the longitudinal displacement pattern at the mid-plane (plane of symmetry in the model). The selected cavities were prepared for metallurgical analysis after the experiment. Different transversal and longitudinal sections of cavities were compared to the simulation results of the same cavity geometry.

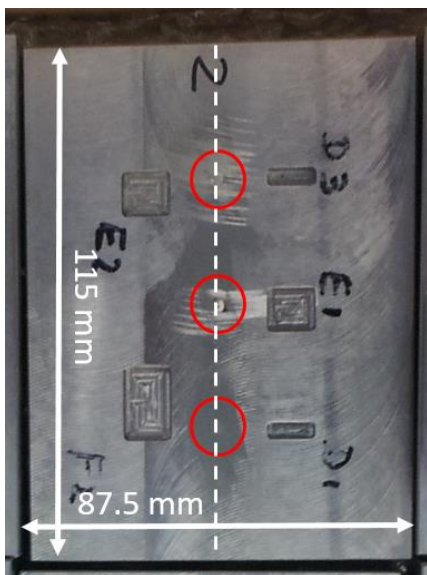


Figure 3: Generic slab sample used to validate the model (top view), pins are highlighted in red.

Further discussion on the selected dimensions of the cavities and experimental procedures can be found in (Nioi *et al.*, 2017). The measured roll forces and the pin distortion were used for comparing the rolling macro-scale model predictions before proceeding to the sub-modelling technique.

5. RESULTS

5.1. Calibration of the material model

The selected Sellars-Tegart model for the studied 3 wt% Si electrical steel was calibrated using flow curves from high temperature compression tests conducted at different temperatures and strain rates.

The high temperature flow curves were measured using a Gleeble 3800 thermomechanical simulator. The material used was production grain-oriented electrical steel grade with the chemical composition of Fe-0.06wt%C-3.1wt%Si-0.16wt%Mn-0.1wt%Cu-0.1wt%Sn and 0.15wt% in total of other minor alloying elements. In the Gleeble, cylindrical samples 8 mm diameter and 18 mm long were tested. The flow stress experiments were isothermal with graphite lubrication to restrict barrelling of the specimen to eliminate friction between the sample and the anvil. Temperature uniformity was maintained within +10C at 1000C and corrected for radiation loss. The Gleeble PID settings were adjusted to obtain strain rates within 10% of the nominal value over the majority of deformation.

Figure 4 shows the experimental flow curves obtained with a Gleeble compression test for different deformation conditions and the model predictions using Eq.(1) for different strain rates and temperatures. The calibrated parameters of Eq.(1) and Eq.(2) are presented in Table 2.

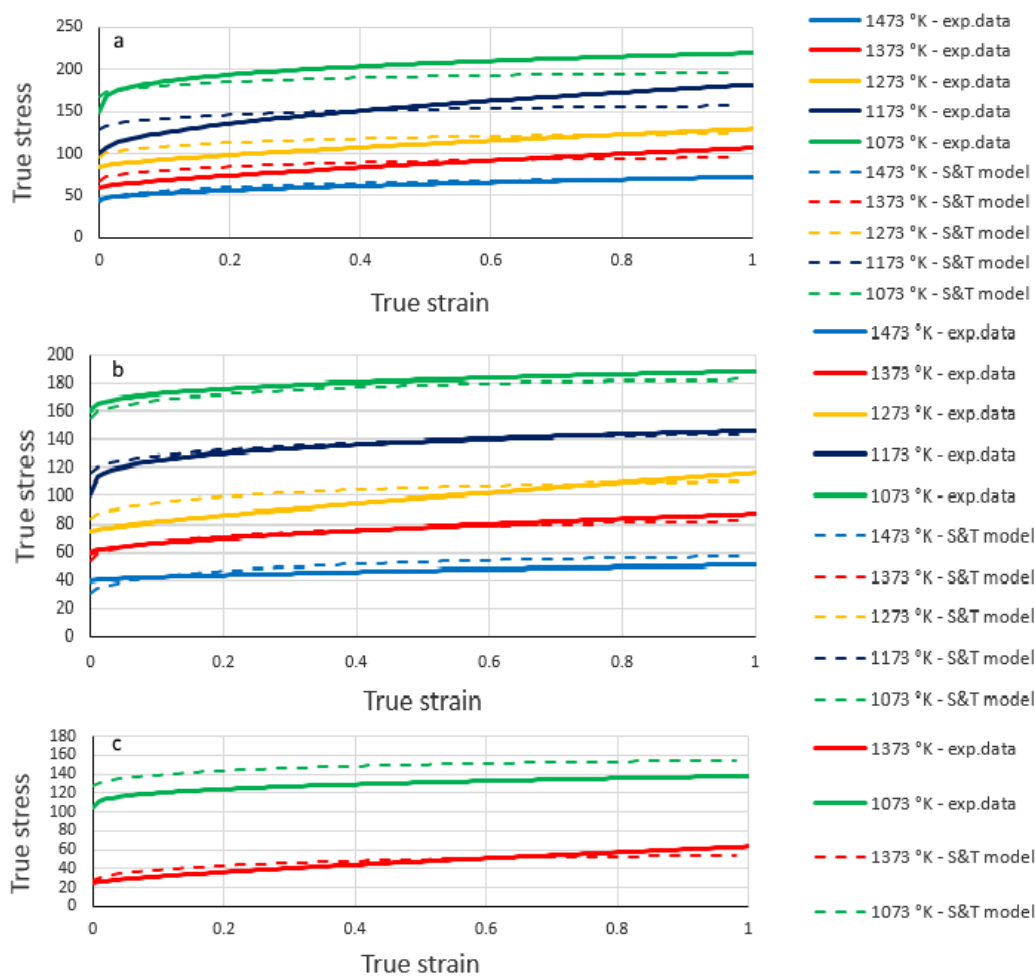


Figure 4: Sellars and Tegart (S&T) model comparison with the experimental data for different strain rates and temperatures (a, b and c stand for hardening curves obtained at strain rates of 25 s⁻¹, 10 s⁻¹ and 1 s⁻¹ respectively).

Table 2: Calibrated material parameters according to the Gleeble compression test results.

Q (MPa)	b	A (s ⁻¹)	α (MPa ⁻¹)	n	ΔH ($\frac{kJ}{mol}$)
23	1.8	$4.6 \cdot 10^{10}$	0.0121	4.223	252.9

The model shows a good agreement with the experimental results for higher values of strain rate (Figure 4a and Figure 4b) with maximum errors being of the order of 10 – 15 %. Higher errors are observed for the lowest temperature and strain rate (800 °C and 1 sec^{-1}). However, the predicted strain rate of deformation during hot rolling in the defect zone is about 10 sec^{-1} and therefore, the model is predicting the material behaviour with reasonable accuracy under operating conditions.

5.2. Validation of Macro-scale model: measured deformation pattern and roll forces

Figure 5 shows an example of a deformed pin after sectioning and polishing of the sample. The contact mechanics and the friction at the interface between the slab and roll were expected to directly influence the distortion of pins (Boldetti *et al.*, 2005). Therefore, an inverse analysis was carried out to calibrate the friction coefficient present during the process. A set of iterative macro-model rolling simulations were conducted with different friction coefficients and the results of the longitudinal displacement patterns were compared to the experimentally determined pin distortion. The simulations reproduced the hot rolling process as explained in (Nioi *et al.*, 2017), to determine the representative friction coefficient in the studied process.

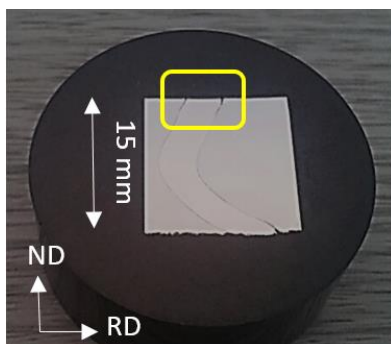


Figure 5: Deformed pin after rolling, longitudinal RD-ND section.

Figure 6 presents a comparison of the top half curvature of the distorted FEM mesh after rolling (presented for different friction values) and the mean distortion of the top half pins observed after the rolling process (dashed line). The curvature is presented from the centre to the contact surface of the slab (half slab). A small deviation from the experimental results was encountered at the surface, as highlighted in red in Figure 6, that could be related to the presence of the highlighted gap between the deformed pin and the slab in Figure 5. According to the results, a friction coefficient of 0.25 provides the best pin distortion prediction compared to the experimental measurements and this value was used for the simulations.

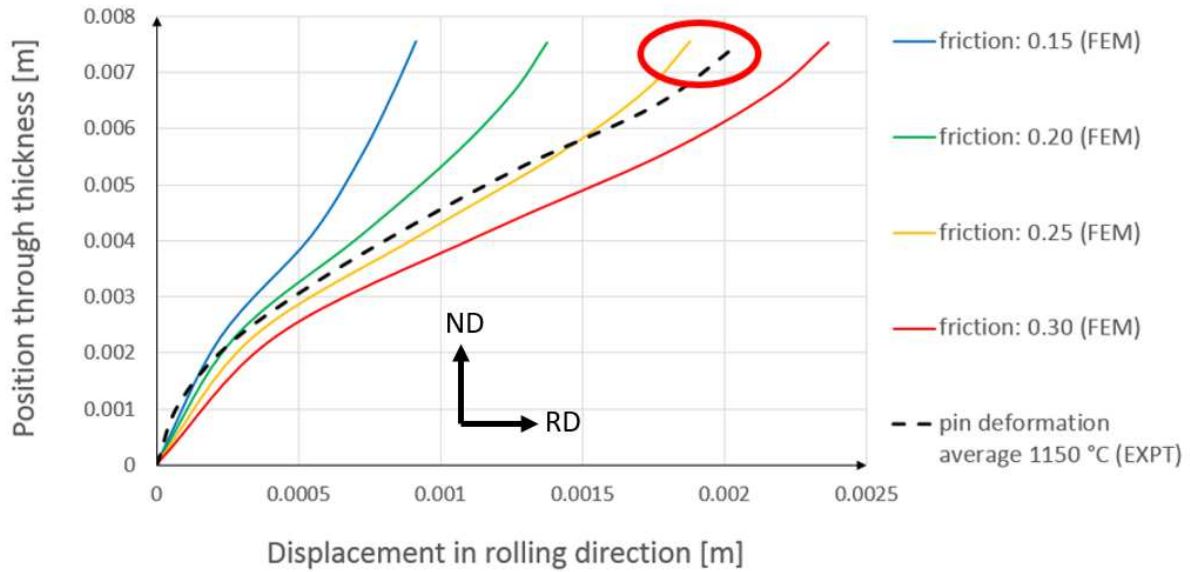


Figure 6: Longitudinal displacement comparison between average pin distortion at 1150°C, and model mesh run at different friction coefficients for the top half of the slab.

Figure 7 shows the measured roll force during the experiment, using a slab with no defect, and the one predicted by a macro-scale model using a friction coefficient of 0.25. The predicted results deviate from the experimentally measured values by about 6%. This has been calculated as the deviation between the average force levels measured during rolling and average of the predicted force levels. In addition, the predicted roll force shows a peak during the first contact between the slab and the roll, as highlighted in Figure 7, which could be due to the transient condition involving the first contact. The predicted increase in the roll force is not expected to affect the defect behaviour as the defects are far from the initial contact point.

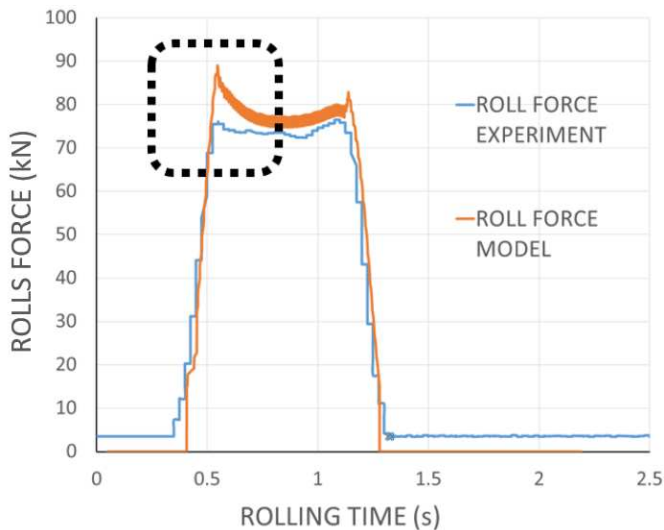


Figure 7: Roll force comparison between experimentally measured values and the model predictions.

5.3. Meso-scale model quality check

The predicted stress and temperature distributions produced by the macro and multi-scale modelling techniques are compared in Figure 8 in order to ensure the latter was properly applied. The results show that there are minor differences in the predicted stress fields around the front edge of the slab far from the embedded defect (as it is highlighted in Figure 8c and d). This difference in the stress distribution could be attributed to the mesh morphology at the corresponding area. Despite the variation in the stress distribution, the predicted temperature fields are similar in both models.

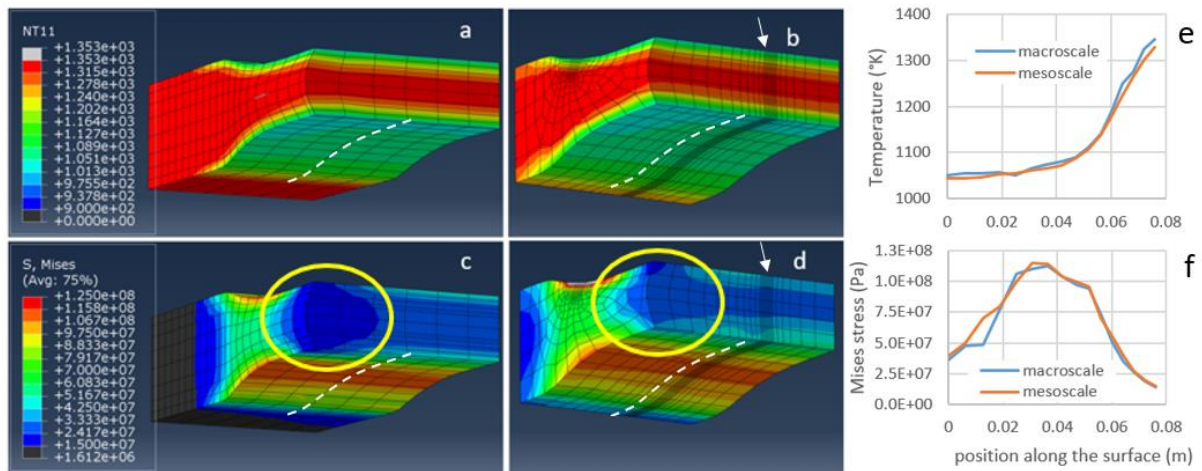


Figure 8: Temperature field ($^{\circ}\text{k}$) comparison between a) macro-scale model and b) meso-scale model; Mises stress comparison (Pa) between c) macro-scale model and d) meso-scale model, next to the boundary surfaces. Plot comparison of e) Temperature and f) Mises stress along the white dashed section on the bottom surface of the slab.

5.4. Prediction of Defect Evolution

The vertical displacement fields on the transversal sections around the selected defects (defects 2, 4 and 5 in Table 3) are shown in Figure 9. These defects have the same initial depth (3mm), so that the effect of the initial cavity aspect ratio could be observed.

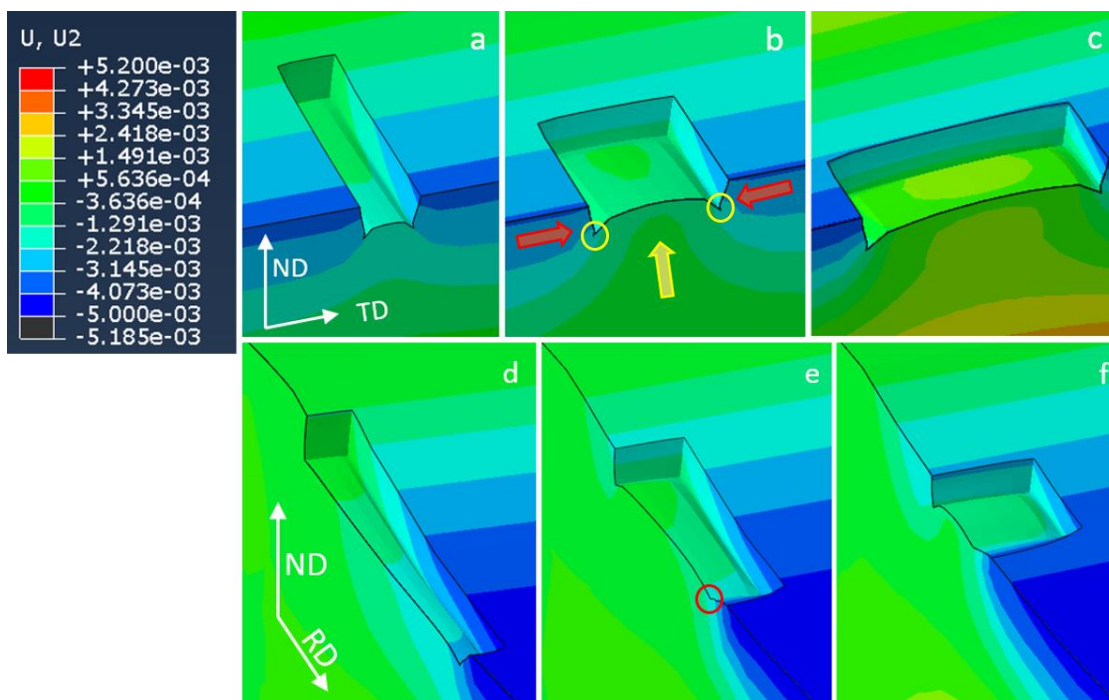


Figure 9: Vertical displacement (m) field for the defects 5 (a), 2 (b), 4 (c) in the transversal section, and 5 (d), 2 (e), 4 (f) in the longitudinal section during rolling. Lateral and vertical spread of the material within the defect is indicated with red and yellow.

The results show that the material was less restricted by the boundaries in the wider cavities that resulted in greater bulging and associated vertical displacements of the bottom surface (defect 4 in Figure 9c compared with defect 2 in Figure 9b). This is shown by the yellow arrow in Figure 9b.

It has been found that crevices, highlighted by the yellow circles in Figure 9b, were formed between the bottom and the lateral side walls of the defects due to the side wall buckling, as indicated by the red arrows in Figure 9b, and by the bulging of the defect floor. A similar effect was also observed at the exit side of the defect in the longitudinal plane, whereas the front wall of the cavity was opened up, as highlighted in Figure 9e. The stress and temperature fields around defects produced by rolling of the selected cavities (cavities 2, 4 and 5 in Table 1) are shown in Figure 10. The figure shows that the boundaries of the defects were cooled down faster than the surroundings. This results in stronger materials and higher local stresses as high as 200 MPa, along the edges of the defects during rolling. The discontinuity in roll-workpiece contact could also contribute to a local stress concentration in the defect corners.

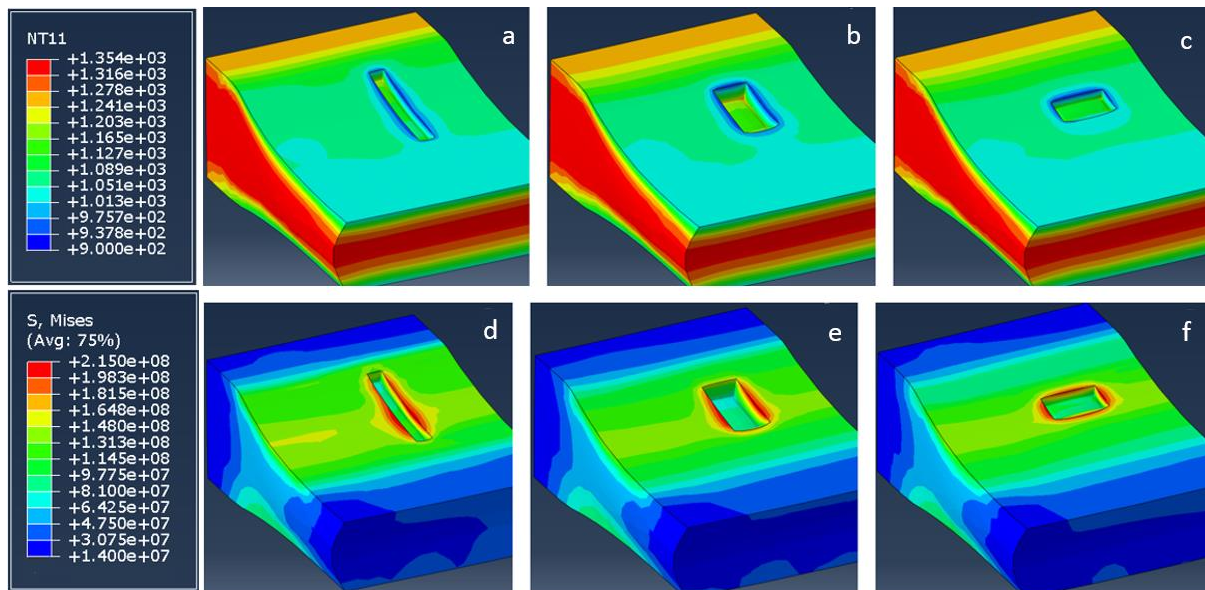


Figure 10: Temperature ($^{\circ}\text{K}$) and stress (Pa) field for the defects 5 (a, d), 2 (b, e), 4 (c, f) during the rolling.

Figure 11 shows the Mises stress distribution at the ND-TD and ND-RD planes for the selected defects in the roll bite. The material is unloaded beneath the surface of the defects due to the bulging effect that is more pronounced for wider cavities as it is shown in Figure 11c and f.

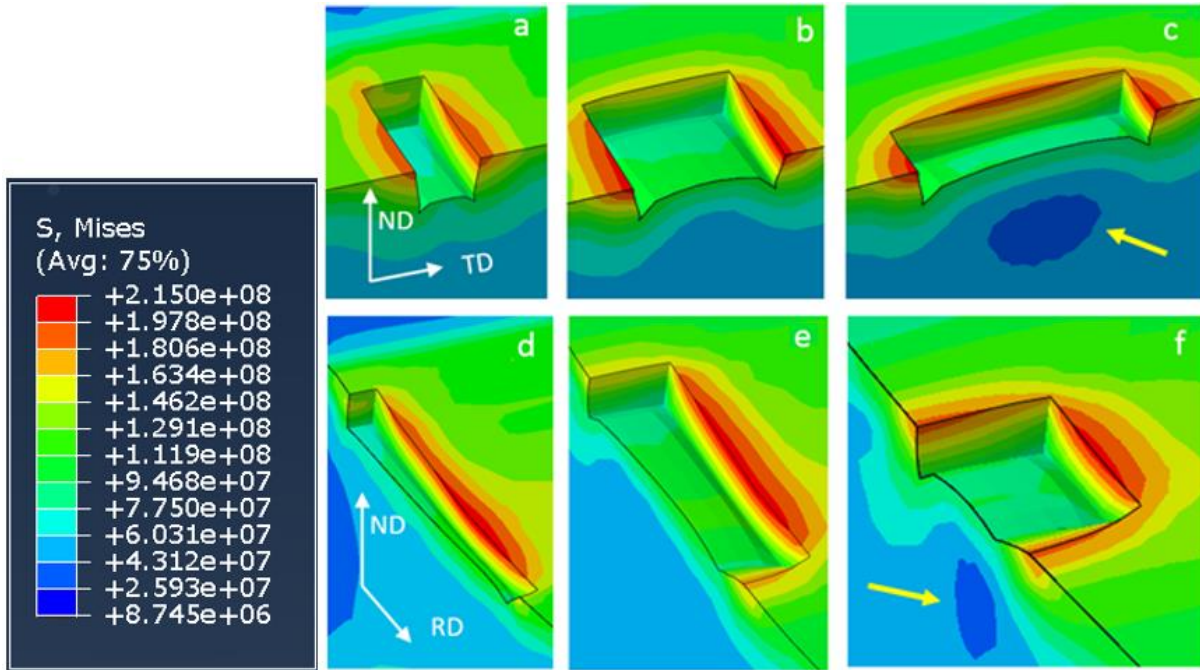


Figure 11: Mises stress (Pa) distribution at transversal and longitudinal sections of defects 5 (a), 2 (b), 4 (c), and longitudinal sections for defects 5 (d), 2 (e), 4 (f).

5.5. Geometrical comparison of the defect morphologies

Figure 12 shows traces of the initial shapes of cavity 2 (broken line) along with the generated defect (solid line) based on the optical micrographs of the defect at TD-ND and RD-ND planes. The final dimensions of measured width (W_f), depth (D_f) and length (L_f) are indicated in Figure 12 (for further information refer to (Nioi *et al.*, 2017)). Figure 12b also shows the effect of the rolling direction on the deformation of the defects where the defect tends to open up in the RD-ND plane due to the interaction with the roll.

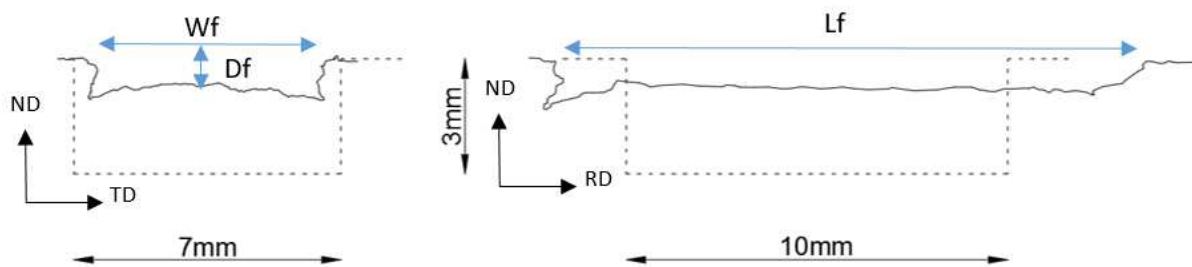


Figure 12: Measurement schematic used to estimate the defect dimensions, transversal (left), and longitudinal (right) sections for a defect (cavity 2). Dashed lines and continuous lines represent the cavity section before and after the rolling respectively. The rolling direction is from left to right in the RD-ND plane.

The predicted deformed geometry of the defects is compared to experimentally measured values along with the associated errors in Figure 13. The simulated results are in good agreement with the experimental measurements for most of the studied defects. The largest differences between the model prediction and the experimentally observed values are for the depth and width of defects 4 and 5. These can be explained from Figure 14 where the predicted transversal shape of the defect 5 is

compared to the experimental result. The discrepancy is due to the under-prediction of the transversal buckling of the side walls of the defect, which may occur due to a different friction coefficient as a result of heterogeneous oxide scale distribution in the experiments (Nioi *et al.*, 2017).

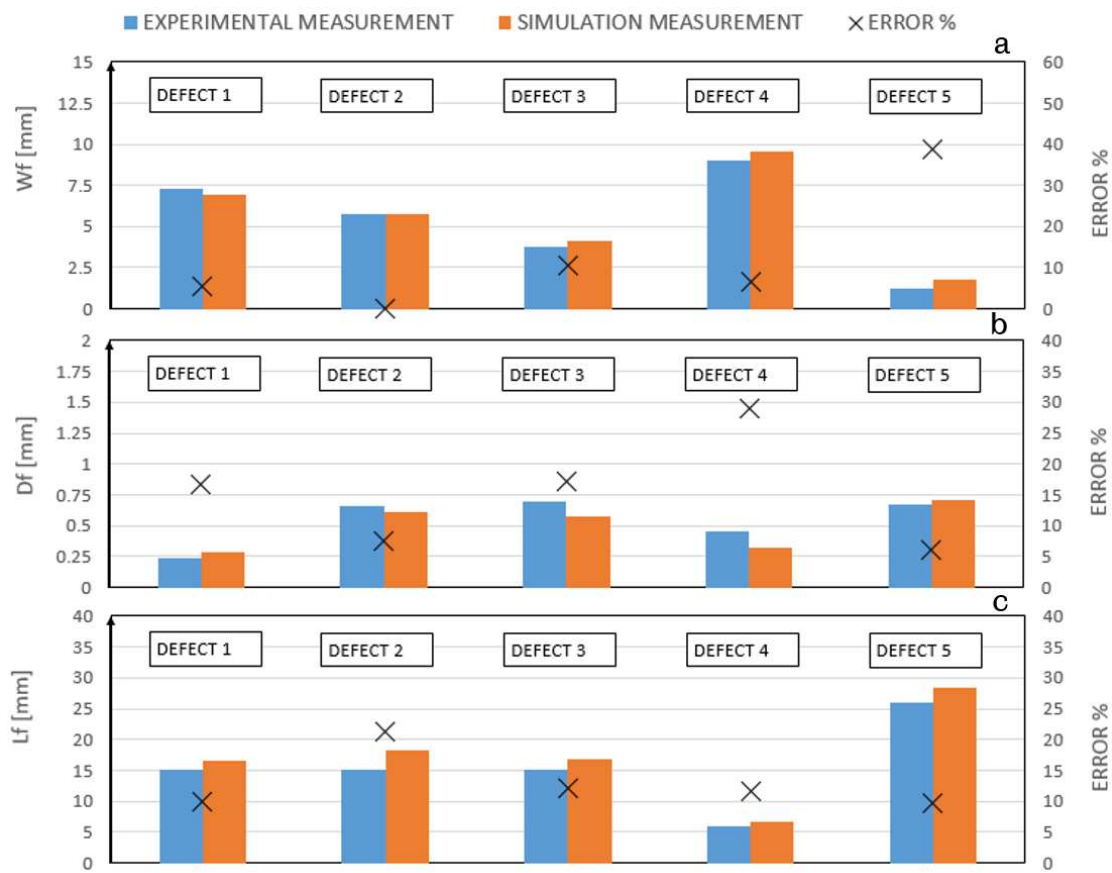


Figure 13: Defect dimensions of width (a), depth (b) and length (c) before and after rolling in experiments compared with those obtained from the simulations. The percentage difference between the model prediction and the experimentally observed values is given by the black crosses with in the right-hand axis.

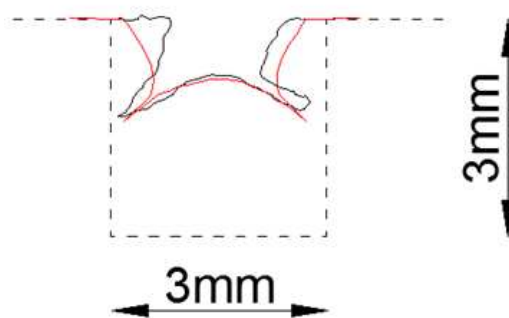


Figure 14: Comparison of the predicted (red line) and the observed (continuous black line) defects sections for cavity C2 in the transversal section (the initial cavity shape is shown by the dashed line).

Figure 15 compares the resulting experimentally observed (right) and modelled geometries (left) of the three defects considered in the transverse and longitudinal sections of Figure 10 and Figure 11. All the defects exhibit a deflection of the side and back walls. The lateral spreading of the material is

highlighted with a red arrow. Although the model predicts well the deformation phenomena apparent from the experiments, there is an under-prediction of the lateral buckling in two cases (Figure 15a and Figure 15c). Slight differences in the shape of the defects corners as highlighted in yellow in Figure 15a are also noted. In the experimental observations, oxide scales inside the defect and in particular at corner crevices were observed for most of the defects, as highlighted with a red rectangle in Figure 15a and b.

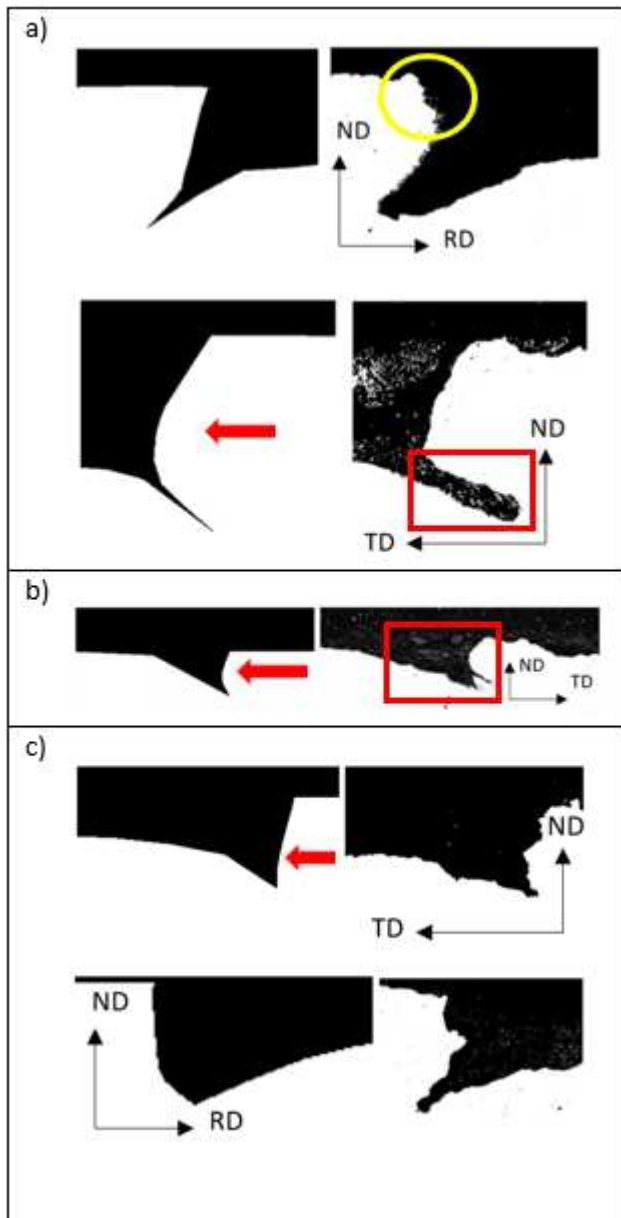


Figure 15: Defect 5 (a), defect 4 (b) and defect 2 (c), sections comparison between simulations (left) and experiments (right). Lateral spreading of the material within the cavity is indicated with red arrows in the transversal section of the defect.

6. DISCUSSION

The sub-modelling technique developed in this work successfully simulated the evolution of surface defects during hot rolling of a high Si-steel. The presence of the defect in the meso-scale model did not substantially affect the stress or the temperature field observed in the macroscale model boundary surfaces, as was shown in Figure 8.

The friction coefficient between roll and slab was calibrated through inverse modelling. Although the analysis of the distorted pin showed some differences in deformation mechanisms between the pin and the sample materials, the advantage of this technique lies in its simplicity and accuracy compared to more complex grid-based techniques (Boldetti *et al.*, 2005). The difference between the experimental observations of the pin compared to the modelled mesh distortion could be due to the detachment at the interface between the pin and the slab as it is highlighted in Figure 5. The obtained friction coefficient of 0.25 is well within the expected range of 0.2-0.4 encountered in the literature (Krzyzanowski *et al.*, 2010). This value was therefore used in all subsequent models.

The observed difference between the measured and predicted roll forces was about 6%, which is an acceptable discrepancy for the following reasons. The heat transfer coefficient value adopted for the simulations is pertinent to hot rolling processes where thin and uniform oxide layers are present due to an effective descaling procedure. However, in the experiments, the surface was prepared immediately prior to rolling by mechanical scraping, which only removed the coarse loose scale. The thicker than expected oxide layer in the experiments may have therefore, reduced the heat transfer between the slab and the roll (Lenard, 1994). It is expected that the model predicts lower internal temperatures and consequently, harder material to deform that requires a higher rolling force. The roll force over-prediction could also be due to the local increase in the material strength during the transient stages of the process. This is due to the fact that an initial velocity boundary condition was applied to the slab to obtain a proper contact with the roll bite when running the macro-scale model. Therefore the strain rate could have been artificially increased resulting in a higher flow stress. As a result, higher roll forces were registered during the initial contact.

The results in Figure 15 show that the model was able to predict crevice forming phenomena in both transversal and longitudinal sections of the defects. According to the simulation results, the main mechanism responsible for this phenomenon is the buckling of the vertical sides and the floor of the defect during the rolling deformation. This is in agreement with the previous publication on modelling of hot rolling conducted by Lee and Choi (2008). Limitations with current predictions are due to the fact that the oxide scale entrapped inside the formed crevices is not accounted for as a separate phase in the model.

While the model did predict the shape of the final defects well, it still miscalculated their final dimensions such that some were 12% longer and wider compared to the experiment (see Figure 13). Since friction is expected to affect the defect evolution during rolling (Krzyzanowski *et al.*, 2010), any local variation in the friction coefficient near and within the cavities due to oxide scale, may affect its evolution. This was not taken into account in the model as only a constant friction coefficient was used for the contact. Anisotropic friction behaviour may also have played a role during the experiment, resulting in different behaviour in the longitudinal and transversal directions, leading to shorter and narrower defects (Krzyzanowski *et al.*, 2010). Another source of error could be the initial geometry of the cavities before rolling (Nioi *et al.*, 2017) by the oxidation during the heating stage. This results in the metallic boundary being slightly enlarged and the corners rounded. The oxide scale could be considered as a separate phase in the model to improve the predicted results. This, however, introduces several challenges for the characterisation of mechanical and tribological properties of the oxide scale. A more accurate control of the oxide scale thickness may be necessary to improve the consistency of the initial assumptions.

Nevertheless, the developed model can be used to predict the final geometry of initially known imperfections in the slabs, or it can be used to carry out a sensitivity analysis of the final defect severity to different process parameters such as friction, temperature, velocity, material properties, reduction ratios etc... . The understanding of the defect evolution mechanisms and the sensitivity of process parameters can be useful to industry in order to prevent or reduce defect formation.

7. CONCLUSIONS

A finite element model was developed to simulate the behaviour of a 3wt% Si steel subjected to hot rolling. This is the first hot rolling simulation of defect behaviour for high Si Steels to the best knowledge of the authors. The stress-strain curves of a Gleeble compression test carried out at different temperatures and strain rates, were adopted to calibrate the Sellars and Tegart model that was implemented in a commercial FE package (ABAQUS) by means of a user-defined subroutine. The selected material model, that did not involve damage softening, was found to be effective in reproducing stress levels at different strain rates and temperatures with a maximum error of 15% in the predicted flow stress of the material.

With regards to the Finite element model, the results obtained can be summarised as follows:

- The multiscale approach was found to be effective for the simulation of relatively small surface indentations during rolling.
- The effect of the oxide scale on friction between roll and slab was taken into account by Coulomb friction coefficient calibration.
- The differences between the predicted and measured roll forces highlighted the importance of the heat transfer coefficients used in the model to obtain more precise results in the predictions.
- The meso-scale models were successfully validated through comparison between the predicted and measured dimensions of the final defects. The errors in the predictions were found to be of about 6% and 12% for the macro-scale and the meso-scale model respectively.
- The most significant finding to emerge from this study is the buckling of the side walls of the defects and the resulting crevice forming phenomena observed. These deformation mechanisms were identified to be the main cause of surface defect generation during rolling and depend on the various aspect ratios and reduction imposed.

To obtain more precise predictions of the defect behaviour, more complex frictional models taking into account possible sticking phenomenon and anisotropic friction values are needed. In addition, a proper modelling of the oxide scale could be very effective in fully describing the subsurface defect formation phenomenon typical of laps and slivers.

8. ACKNOWLEDGMENTS

The project was partly funded by Tata Steel Europe. Technical support of Tata Steel Europe is also greatly acknowledged.

9. REFERENCES

- Abaqus, 6.13, Documentation manual. Dessault Systèmes 2013.
- Baragar, D. L. The high temperature and high strain-rate behaviour of a plain carbon and an HSLA steel. *Journal of Mechanical Working Technology*, v. 14, n. 3, p. 295-307, 1987. ISSN 0378-3804.
- Boldetti, C. et al. Measurement of deformation gradients in hot rolling of AA3004 C. *Experimental Mechanics*, v. 45, 2005.
- Brown, S.; Kim, K.; Anand, L. An internal variable constitutive model for hot working of metals. *International Journal of Plasticity*, v. 5, n. 2, p. 95-130, 1989. ISSN 0749-6419.
- Chen, R. Y.; Yuen, W. Y. D. Oxide-Scale Structures Formed on Commercial Hot-Rolled Steel Strip and Their Formation Mechanisms. *Oxidation of Metals*, v. 56, n. 1, p. 89-118, 2001.
- Grenier, C. et al. Behaviour of oxide scales in hot steel strip rolling. *International Journal of Material Forming*, v. 1, n. SUPPL. 1, p. 1227-1230, 2008.
- Krzyzanowski, M.; Beynon, J. H.; Farrugia, D. C. Oxide scale behaviour in high temperature metal processing. John Wiley & Sons, 2010. ISBN 3527630325.
- Lee S.-J, Choi J.-W Deformation analysis of surface defect on hot rolling by 3-D FEM simulation. *Revue de Metallurgie. Cahiers D'Informations Techniques*, v. 105, n. 3, p. 127-135+III-IV, 2008.
- Lenard, J. G. An Experimental Study of Boundary Conditions in Hot and Cold Flat Rolling. *CIRP Annals* n. 1, p. 279-282, 1990.
- Lenard, J.G. A study of the heat-transfer coefficient as a function of temperature and pressure. *Journal of Materials Processing Technology*, v. 41, p. 125-142, 1994.
- Li, Y. H.; Sellars, C. M. Comparative investigations of interfacial heat transfer behaviour during hot forging and rolling of steel with oxide scale formation. *Journal of Materials Processing Technology*, v. 81, p. 282-286, 1998.
- Munther, P. A.; Lenard, J. G. The effect of scaling on interfacial friction in hot rolling of steels. *Journal of Materials Processing Technology*, v. 88, p. 105-113, 1999. ISSN 1519888619.
- Nioi, M. et al. Surface defect evolution in hot rolling of high-Si electrical steels. *Journal of Materials Processing Technology*, v. 249, p. 302-312, 11// 2017. ISSN 0924-0136.
- Onishi, T.; Nakakubo, S.; Takeda, M. Calculations of Internal Oxidation Rate Equations and Boundary Conditions between Internal and External Oxidation in Silicon Containing Steels. *Materials Transactions* v. 51, n. 3, p. 482-487, 2010.

Rodriguez-Calvillo, P. et al. On the hot working of FeSi ferritic steels. *Materials Science and Engineering: A*, v. 606, p. 127-138, 2014.

Sellars, C. M.; Tegart, W. J. M. Hot Workability. *International Metallurgical Reviews*, v. 17, n. 1, p. 1-24, 1972.

Shangwu, X. et al. Three-dimensional thermo-mechanical finite element simulation of the vertical–horizontal rolling process. *Journal of Materials Processing Technology*, v. 110, n. 1, p. 89-97, 2001.

Song, E. J.; Suh, D. W.; Bhadeshia, H. K. D. H. Oxidation of silicon containing steel. *Ironmaking and Steelmaking* v. 39, n. 8, p. 599-604, 2012.

Sun, W. A study on the characteristics of oxide scale in hot rolling of steel. University of Wollongong Australia, PhD Thesis, p. 228-228, 2005.

Suárez, L. et al. Oxidation of ultra low carbon and silicon bearing steels. *Corrosion Science*, v. 52, n. 6, p. 2044-2049, 2010.

Takeda, M. et al. Physical Properties of Iron-Oxide Scales on Si-Containing Steels at High Temperature. *Materials Transactions*, v. 50, n. 9, p. 2242-2246, 2009.

Tello, K. E.; Gerlich, A. P.; Mendez, P. F. Constants for hot deformation constitutive models for recent experimental data. *Science and Technology of Welding & Joining*, 2013.

Utsunomiya, H. et al. Deformation of oxide scale on steel surface during hot rolling. *CIRP Annals* v. 58, p. 271-274, 2009.

Uvira J.L, Jones J. J. Hot compression of Armco iron and silicon steel. *Transactions of the Metallurgical Society of AIME*, v. 242, n. October 1967, p. 1619-1926, 1968.

Yu, H.-L.; Liu, X.-H. Thermal – Mechanical Finite Element Analysis of Evolution of Surface Cracks During Slab Rolling. *Materials and Manufacturing Processes* v. 6914, n. March, 2016.

Yu, H.-L. et al. Deformation behavior of inclusions in stainless steel strips during multi-pass cold rolling. *Journal of Materials Processing Technology*, v. 9, p. 455-461, 2008.